NeuroImage 88 (2014) 10–21

Contents lists available at ScienceDirect

NeuroImage

journal homepage: www.elsevier.com/locate/ynimg

The dynamics of contour integration: A simultaneous EEG–fMRI study

Bogdan Mijović [a,b,*], Maarten De Vos [a,d], Katrien Vanderperren [a,b], Bart Machilsen [c], Stefan Sunaert [e], Sabine Van Huffel [a,b], Johan Wagemans [c]

[a] KU Leuven, Department of Electrical Engineering, STADIUS, Leuven, Belgium
[b] KU Leuven, iMinds Future Health Department, Leuven, Belgium
[c] KU Leuven, Laboratory of Experimental Psychology, Leuven, Belgium
[d] Oldenburg University, Department of Psychology, Neuropsychology Lab, Oldenburg, Germany
[e] KU Leuven, Department of Radiology, Leuven, Belgium

ARTICLE INFO

Article history:
Accepted 14 November 2013
Available online 21 November 2013

Keywords:
Contour integration
Shape detection
Vision
EEG–fMRI integration
Data driven methods

ABSTRACT

To study the dynamics of contour integration in the human brain, we simultaneously acquired EEG and fMRI data while participants were engaged in a passive viewing task. The stimuli were Gabor arrays with some Gabor elements positioned on the contour of an embedded shape, in three conditions: with local and global structure (perfect contour alignment), with global structure only (orthogonal orientations interrupting the alignment), or without contour. By applying JointICA to the EEG and fMRI responses of the subjects, new insights could be obtained that cannot be derived from unimodal recordings. In particular, only in the global structure condition, an ERP peak around 300 ms was identified that involved a loop from LOC to the early visual areas. This component can be interpreted as being related to the verification of the consistency of the different local elements with the globally defined shape, which is necessary when perfect local-to-global alignment is absent. By modifying JointICA, a quantitative comparison of brain regions and the time-course of their interplay were obtained between different conditions. More generally, we provide additional support for the presence of feedback loops from higher areas to lower level sensory regions.

© 2013 Elsevier Inc. All rights reserved.

Introduction

To successfully interact with the environment our brain transforms the pattern of light on the retina into meaningful and coherent representations of the objects, scenes and events in the world. To decide which parts of the visual input belong together, and which parts belong to separate objects or to the background, our visual system relies on grouping principles such as proximity, similarity, and collinearity. These grouping principles have been introduced by the Gestalt psychologists early last century (for review, see Wagemans et al., 2012), and reflect the statistical properties of our natural environment (Elder and Goldberg, 2002; Geisler, 2008).

In the present study we investigate the neural mechanisms underlying the grouping principle of collinearity or "good continuation" (Wertheimer, 1923) in shape perception: the tendency to link spatially aligned neighboring elements into a continuous string. This process, referred to as contour integration, is crucial to detect borders between distinct image regions. An effective method for studying contour integration is the pathfinder or snake detection paradigm (Field et al., 1993), which requires participants to detect a smooth contour in a background of randomly positioned Gabor elements. Psychophysical studies have demonstrated that contour integration depends on the separation and orientation of the local elements relative to the global path trajectory (Hess and Field, 1999).

Some authors have argued that a reinforcing cascade of lateral connections between orientation tuned cells in the primary visual cortex (V1) provides the neural substrate for contour integration (e.g., Li and Gilbert, 2002). However, a serial propagation through intrinsic horizontal connections in V1 might be too slow to account for fast modulatory influences by stimuli far outside the classical receptive field of V1 cells (Angelucci and Bressloff, 2006). Most likely, contour integration is mediated partly by extrastriate feedback connections to V1 (Angelucci et al., 2002). This feedback from higher visual areas could also explain the sensitivity of V1 neurons to the shape of spatially extended contours (McManus et al., 2011), especially when the contours form closed shapes.

The contribution of both striate and extrastriate areas to contour integration has also been observed in functional magnetic resonance imaging (fMRI) studies. Gabor elements that are arranged in closed shapes elicit stronger BOLD responses than randomly oriented Gabor elements, in the object-sensitive lateral occipital complex (LOC) as well as in early visual areas (Altmann et al., 2003; Kourtzi et al., 2003), suggesting a feedback mechanism from higher to lower visual areas. Although fMRI can inform us about which cortical areas are involved in contour integration, it does not allow tapping into the temporal aspects of the grouping processes, and the dynamic interplay between

* Corresponding author at: Kasteelpark Arenberg 10, Box 2446, B-3001 Leuven, Belgium. Fax: +32 16321970.
E-mail address: bogdan.mijovic@esat.kuleuven.be (B. Mijović).

1053-8119/$ – see front matter © 2013 Elsevier Inc. All rights reserved.
http://dx.doi.org/10.1016/j.neuroimage.2013.11.032

feedforward and feedback processes. Electro-encephalography (EEG) and magneto-encephalography (MEG), on the other hand, have good temporal resolution but insufficient spatial precision.

The goal of the current study was to identify fine spatiotemporal interactions between the different cortical regions involved in contour integration and shape detection, and to provide further evidence for feedback from LOC to early visual regions, by exploiting simultaneous EEG–fMRI measurements. A critical aspect of this study, compared to previous work, is that we have combined contour integration with shape detection, and that we have compared conditions in which local element linking is part of contour integration with conditions in which the contour of a global shape emerges only at a higher level.

Materials and methods

Participants

Fifteen participants (eight male, seven female; mean age 27.4 years) with no history of neurological or cardiological disorders volunteered for this study. All participants reported normal or corrected-to-normal vision and gave written informed consent. The study was approved by the KU Leuven Ethics Committee.

Stimuli and conditions

We used MATLAB (v 7.1; The MathWorks, Natick, MA, USA) and GERT, the Grouping Elements Rendering Toolbox (Demeyer and Machilsen, 2012), to construct arrays of non-overlapping Gabor elements on a uniform gray background (Fig. 1). The arrays comprised 496 × 496 pixels. During the experiment the arrays were presented centrally and subtended approximately 10° of visual angle. Each Gabor element was defined as the product of a sine wave luminance grating (frequency of 3 cycles per degree of visual angle) and a circular Gaussian (standard deviation of 3 arc min). A subset of 45 Gabor elements was positioned along the contour outline of an artificial shape.

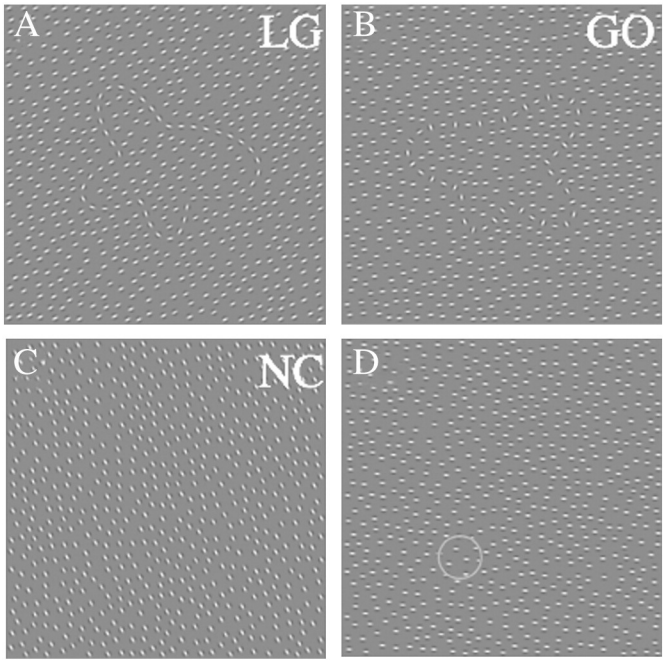


Fig. 1. Example stimuli used in the experiment. (A) *Local and global* stimulus, obtained by orienting the elements on the contour parallel to the local tangent at the contour. (B) *Global only* stimulus, in which every other contour element alternates between an orientation parallel to or orthogonal to the shape outline. (C) *No contour* stimulus, in which all Gabor elements have the same orientation. (D) *Catch* stimulus, which is always a no-contour stimulus with a small circle overlaid at a random location. Catch trials are not included in the analyses.

The shape outlines were generated by plotting the sum of 5 radial frequency components in polar coordinates, with each component having a random phase angle and amplitude. After rescaling the surface area to one eighth of the array size we co-localized the center of mass of each shape with the center of the array. This procedure yielded shapes of intermediate complexity, not too homogenously convex but also not with too many salient protrusions or indentations.

Next, the remainder of the array was populated with Gabor elements. The number of elements inside and outside the shape outline was adjusted for each shape to ensure a homogeneous spacing between the Gabor elements. The number of interior elements ranged between 60 and 72, the number of exterior elements between 507 and 542. No stimuli were included for which the mean local density – here defined as the average Euclidean distance from each element to its five nearest neighbors – differed more than 1 arc min between interior, contour, and exterior elements. This procedure yielded displays with uniform element density, which necessitates grouping based on element orientation.

In each array all interior and exterior elements had the same orientation. Three different stimulus types were obtained by manipulating the orientations of elements on the contour (Fig. 1). In the *local and global* (**LG**) condition (panel A), all contour elements were aligned along the outline of the embedded shape. In other words, each pair of adjacent contour elements is *locally* aligned, and the entire set of contour elements results in a perceptually closed *global* shape. In that condition, local edge linking at a lower level could give rise at an integrated shape percept at a higher level. In the *global only* (**GO**) condition (panel B), only half of the contour elements were aligned along the outline of the embedded shape and every other element was oriented perpendicular to the shape outline. This still yields a global percept of a closed contour, albeit somewhat weaker, but without the local alignment between adjacent contour elements. In other words, in this condition, local edge linking is made impossible and the global shape can only emerge at a higher level, either by linking only every other element (requiring orientation coupling across larger distances) or by treating the local elements only as place markers while ignoring the orientation of half of the elements. In the *no contour* (**NC**) condition (panel C), all elements on the embedded shape outline were oriented parallel to the other elements in the array, giving rise to a uniform texture with no visible contour or shape.

Task and procedure

Participants engaged in a passive viewing task. They fixated in the middle of the screen while the stimuli were displayed on a uniform gray background. To ensure that participants attended the displays we introduced an undemanding orthogonal catch task. Participants were instructed to press a response button when a circle was present in the array (Fig. 1D). The location of the circle varied across catch trials. Catch trials were not included in the analyses.

An experimental run lasted about 5 min, and consisted of contour trials (frequency = .24), no contour trials (frequency = .48), catch trials (frequency = .08), and blank trials (dummy trials) in which no stimuli were presented at all (frequency = .20). There were exactly 120 structure trials, 240 non-structure trials, 40 catch trials and 100 blank trials per condition (LG | GO). LG and GO conditions were presented in separate runs, 4 of each type. The stimulus order within each run was optimized using the approach suggested by Kao et al. (2009). A GO or LG contour stimulus was always preceded by 1 to 5 NC stimuli with identical Gabor positions, and was always followed by a NC stimulus with different Gabor positions. All the NC stimuli had different orientations of Gabor elements and we therefore do not expect any low-level adaptation to the NC stimuli. To make sure that any effect pertains only to differences in element orientation (and not to differences in element position), the first NC stimulus following a GO or LG contour stimulus was not included in our analyses. The positions of Gabor

elements in successive NC arrays did not change, but their orientations did (each element was rotated at least 30° away from its previous orientation).

Each stimulus was presented for 200 ms. The duration of the inter-trial interval was uniformly sampled between 2000 and 2400 ms. A central fixation cross was shown during the inter-trial interval. The experiment was run with the Presentation software (Neurobehavioral Systems, Albany, CA, USA). A Barco 6400i LCD projector was used to present the stimuli on a translucent screen attached to the bore of the scanner. Participants saw the stimuli via a mirror attached to the head-coil.

Functional MRI

fMRI acquisition

To acquire the functional MRI (fMRI) data we used a Philips 3-T Intera scanner (Royal Philips Electronics, Amsterdam, the Netherlands) with an eight-channel SENSE head-coil. For each experimental run 155 echo-planar images (EPI) were recorded with 2 s repetition time (TR) and 30 ms echo time (TE). To ensure whole-brain coverage each EPI contained 36 slices of $3 \times 3 \times 3$ mm voxel size. In addition to the EPIs, a full brain anatomical image was obtained with the magnetization-prepared rapid acquisition with gradient echo (MP-RAGE) imaging sequence (182 coronal slices, TR = 9.7 s, TE = 4.6 ms, $1 \times 1 \times 1$ mm voxel size).

fMRI preprocessing

fMRI analyses were performed with the statistical parametric mapping software (SPM8, Wellcome Trust Centre for Neuroimaging, London, UK). The EPIs were slice-time corrected, realigned, co-registered with the MP-RAGE, and then normalized to MNI space using the ICBM152 T1-weighted template, and smoothed with a 6-mm FWHM Gaussian kernel. Next, fMRI activation maps were obtained via a general linear model (GLM) analysis with stick-functions based on the onset times of the different stimuli. The stick functions were used to model each condition separately. The stick functions are then convolved with the canonical HRF (double gamma) as implemented in SPM8 package to obtain the final regressors. More specifically, the percent signal change (PSC) data were computed voxel-wise from the betas estimated in the single subject single task GLM analysis as a voxel's condition specific beta weight relative to its session specific beta weight. The PSC computation is done according to Eq. (1) in the same way as the percent local signal change was computed in Gläscher, 2009. The unthresholded PSC maps were the input for the subsequent JointICA analysis.

$$PSC = (\beta_{max} \cdot max(HRF) \cdot 100)/\beta_{const} \quad (1)$$

Localizer runs

In addition to the 8 experimental runs focusing on contour integration, we ran 4 localizer runs, designed to accurately define a number of retinotopic and shape-selective brain areas that we assume to be involved in the visual processing of our contour integration stimuli. The acquisition parameters differed slightly from the experimental runs. For the localizer runs we recorded 110 EPIs with 48 slices at a TR of 3 s and a TE of 30 ms.

Two runs were used to localize early visual areas V1 and V2 with a standard meridian mapping technique. Horizontal and vertical wedges composed of checkerboard and circular patterns were presented to the participants. The patterns alternated at 2.66 Hz. These stimuli specifically activate the borders between early retinotopic areas. In the remaining two localizer runs we presented intact and scrambled versions of familiar objects. Each stimulus was presented for 750 ms. The contrast between intact and scrambled images can be used to extract the lateral occipital complex, an occipitotemporal region involved in the representation of a perceived object shape (e.g., Grill-Spector et al., 1998).

Definition of regions of interest

To define the regions of interest (ROIs), the anatomical images of all participants were first segmented and flattened using the caret5 software (Van Essen Laboratory, Washington University, St. Louis, USA). Subsequently, SPM contrast maps from the object-localizer and meridian-mapping runs were projected on these flat maps, and thresholded based on a p-value of 0.001. The resulting overlays allowed defining the LOC (including the lateral occipital cortex, LO, and the posterior fusiform gyrus, pFs) for the object-localizer runs, and areas V1 and V2 for the meridian-mapping runs. Group ROIs were defined as the region where the individual ROIs from at least 10 participants spatially overlapped.

Electrophysiology

EEG acquisition

The EEG data were collected in the scanner from 62 standard scalp sites using the MR-compatible BrainAmp MR + system (BrainProducts, Munich, Germany), at a sampling rate of 5 kHz. Two additional electrodes were placed below the left eye and on the left upper back to monitor eye blinks and the electrocardiogram, respectively. All 64 channels were recorded with FCz as reference and Iz as ground. Electrode impedances were kept below 10 kΩ. The clock of the MR system was down-sampled to pace the clock of the EEG acquisition computer using commercially available hardware (SyncBox, Brain Products). The start of each volume was automatically marked in the EEG data.

EEG preprocessing

Preprocessing of the raw EEG data was done in the EEGLAB software (v. 5.03; Delorme and Makeig, 2004). First, scanner-related gradient artifacts were reduced with the average template subtraction method (Allen et al., 2000), as implemented in the Bergen EEG–fMRI EEGLAB plug-in (Moosmann et al., 2009). After filtering the data between 1 and 30 Hz and downsampling to 250 Hz, scanner-related ballistocardiogram artifacts were reduced with a combination of the Optimal Basis Set method (Niazy et al., 2005) and ICA (Vanderperren et al., 2010). In addition, eye movement artifacts were reduced with ICA (De Vos et al., 2011; Joyce et al., 2004), all the removed components were manually checked, and data were re-referenced to the average of TP9 and TP10 (the electrodes closest to the mastoids in our electrode setup).

To extract event-related potentials (ERPs), all available blocks per participant and per condition were merged together and data were segmented from 100 ms before until 500 ms after stimulus onset. Baseline correction was performed based on the 100 ms pre-stimulus interval and low quality trials were rejected by thresholding trials at 150 μV. Finally, an average ERP for each stimulus type was computed.

Using the above-mentioned methods, the scanner-related artifacts in the ERP are significantly reduced. We provide the plots of the average ERP's together with the standard deviations in the top panel of Fig. 2. From this figure, it is apparent that a sufficient artifact reduction from the ERP data has been achieved to allow for further processing.

Data analysis Part I — Joint ICA for each stimulus category

To extract spatio-temporal information from the simultaneously acquired EEG and fMRI data different data integration approaches can be applied. For a consistent overview, we refer the reader to Huster et al. (2012). In this work we make use of JointICA, a principled and data-driven approach to multimodal data integration. The technique was originally introduced by Calhoun et al. (2006), and has recently been validated by Mijović et al. (2012). JointICA starts from the assumption that encephalographic and hemodynamic responses co-vary.

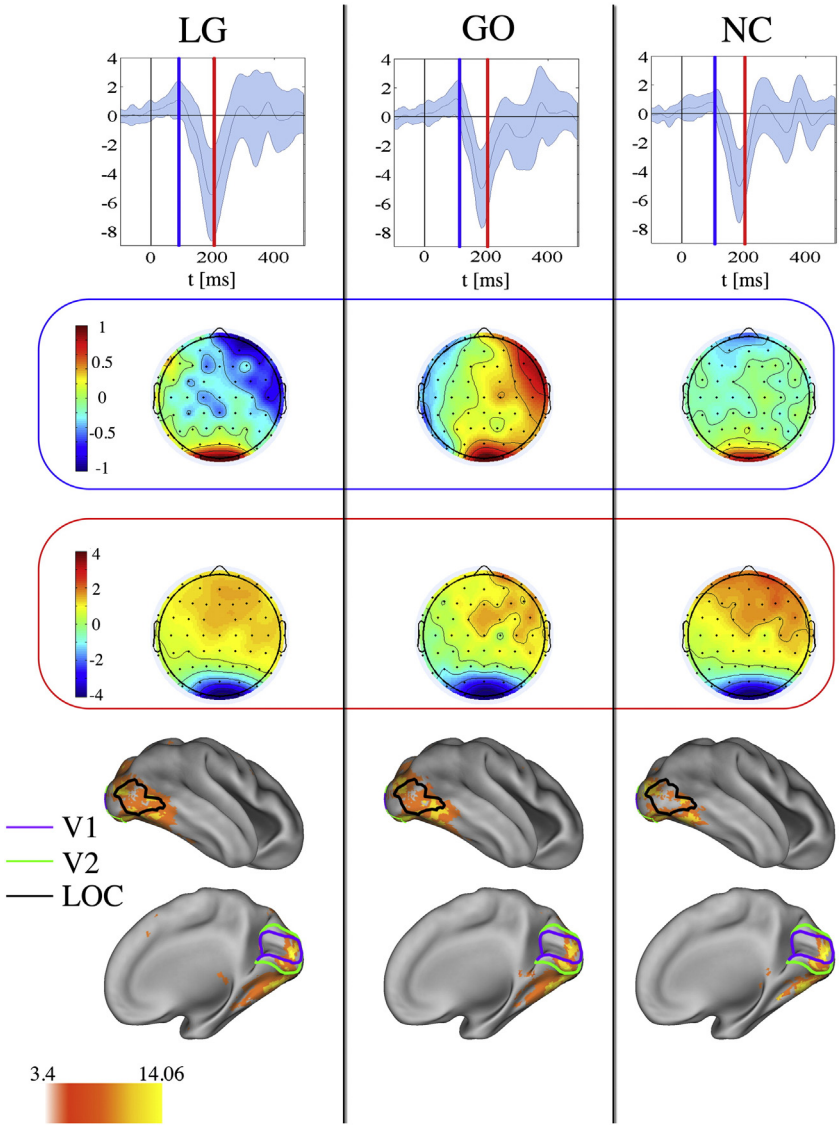


Fig. 2. Top panel: Condition-specific grand average (N = 15) ERPs (LG = local and global; GO = global only; NC = no contour) on channel Oz. The shaded area represents the standard deviation across subjects. The vertical axes in both ERP and scalp maps are given in microvolts. Middle panel: Scalp distributions at the 2 time points indicated by the vertical lines in the top panel: around 90 ms (blue, top) and around 190 ms (red, bottom) after stimulus onset. Bottom panel: Results from a 2nd-level SPM analysis on the fMRI data, showing the effect of each condition relative to fixation ($p = 0.01$, uncorrected), together with the group ROIs V1, V2 and LOC. The color bar describes the T-values of the functional maps. These group ROIs are defined as the region of overlap between individual ROIs from at least 10 out of 15 participants.

To apply the JointICA we first vectorized the fMRI PSC map for every participant and stimulus condition and concatenated this with the average ERP at a specific channel for the same participant and stimulus condition. The vectors were approximately 150,000 samples long (the ERP data were upsampled to fit the length of the fMRI data). The data were Z-transformed. The ERP and fMRI data were normalized separately. We always used electrode Oz as the channel of interest, as this occipital electrode appears to be well-suited for the analysis of visual processes with JointICA (Mijović et al., 2012). This electrode was chosen for 2 main reasons: 1) It is centrally suited, so it measures the activity in both left and right cortex equally, and 2) From Mijović et al. (2012), where PO7 and PO8 electrodes were also explored, Oz was the only electrode to be able to unravel the activity in EVA, which is crucial in this study. We then built for each condition a matrix with the subject-specific concatenated fMRI-EEG vectors as rows. This matrix was demixed using the JointICA algorithm (freely available from http://icatb.sourceforge.net), resulting in joint independent component maps as in Eq. (2). These joint independent component maps incorporate both spatial and temporal information about the neural sources involved in processing of our stimuli.

$$\left[X^{fMRI}\ X^{EEG}\right] = \mathrm{A} \cdot \left[s^{fMRI}\ s^{EEG}\right] \tag{2}$$

After estimating the mixing matrix A, the sources can be extracted by

$$s = \mathrm{A}^{-1} \cdot X. \tag{3}$$

Next, the sources of interest are selected based on their energy contribution, such that the selected sources together explain more than 85% of the total energy in both ERP and fMRI modalities. Finally, the back-reconstruction of a particular source was achieved by simply setting all other sources to zero, and computing X_{br} as

$$X_{br} = \mathrm{A} \cdot s_i. \tag{4}$$

The reliability of the JointICA decomposition was checked by calculating the stability index (*Iq*) using ICASSO (Himberg et al., 2004), as proposed by Mijović et al. (2012). The *Iq* index was computed for all independent components, both based on the complete dataset (15 participants), and when one of the participants was left out. In addition, this ICASSO analysis allowed us to estimate the number of underlying components, based on the computation of the R-index (Himberg et al., 2004). A reliability index higher than 0.9 implies a robust decomposition (Mijović et al., 2012).

Data analysis Part II — Simultaneous JointICA for all stimulus categories together

In the above analysis we performed the traditional JointICA on the data of each condition separately. However, our three stimulus conditions and the processes induced by them show certain similarities, and hence it can be expected that they share some underlying neural sources. A separate demixing for each stimulus condition makes it difficult to identify the common sources, and at the same time complicates the extraction of unique, condition-specific sources. It would therefore be advantageous to estimate the mixing matrices and sources for all three conditions simultaneously. As such, this modified JointICA can reveal the similarities and peculiarities between conditions.

To explain our approach in more detail, let us denote the matrices representing the EEG and fMRI data from all participants, induced by condition LG, with X_{LG}^{EEG} and X_{LG}^{fMRI}, respectively (and analogously for the conditions GO and NC). We then combine the data from the different conditions in a single matrix and perform the ICA analysis, as shown in Eq. (5):

$$\begin{bmatrix} X_{LG}^{fMRI} & X_{LG}^{EEG} \\ X_{GO}^{fMRI} & X_{GO}^{EEG} \\ X_{NC}^{fMRI} & X_{NC}^{EEG} \end{bmatrix} = \begin{bmatrix} A_{LG} \\ A_{GO} \\ A_{NC} \end{bmatrix} \cdot \begin{bmatrix} s^{fMRI} & s^{EEG} \end{bmatrix} \tag{5}$$

with A_{LG}, A_{GO} and A_{NC} the parts of the mixing matrix A corresponding to the conditions LG, GO and NC, respectively, and s^{EEG} and s^{fMRI} the EEG and fMRI portions of the extracted independent components. For similar processes across conditions, the A_{LG}, A_{GO} and A_{NC} parts of the mixing matrix will be similar for the three conditions. For a process unique to a specific condition, the mixing coefficients of this particular condition will differ from the other two conditions. This modification of the JointICA algorithm assesses the information embedded in the source signals jointly for all conditions.

We can then use the condition-specific parts of the estimated mixing matrix to back-reconstruct the sources for a particular condition. For example, by multiplying the inverse of the LG-specific part of the mixing matrix A with the EEG and fMRI data from this same condition, the independent sources for the LG condition can be extracted. This is illustrated in Eq. (6), where A_{LG}^{-1} is the pseudo-inverse of the LG-specific part of the mixing matrix.

$$\begin{bmatrix} s_{LG}^{fMRI} & s_{LG}^{EEG} \end{bmatrix} = A_{LG}^{-1} \cdot \begin{bmatrix} X_{LG}^{fMRI} & X_{LG}^{EEG} \end{bmatrix} \tag{6}$$

As before, we use the energy criterion to disregard noise components. Next, we can detect which sources are common to two or three conditions and which ones are unique to a single condition by comparing the distribution coefficients of a particular independent component across subjects. If the component's distribution coefficients are significantly higher in one condition compared to the other conditions, we conclude that this particular component is unique to this condition. If the component shows a similar distribution across subjects for two or more conditions, we conclude that this process is common for these conditions. Statistical significance is formally tested using paired *t*-tests.

Results

We first present the results of a traditional, single-modality analysis of our EEG and fMRI data, as if the data for each modality were acquired in a separate session. Next, we describe the results of a multimodal analysis of EEG and fMRI data using JointICA. Finally, we apply our modification of the JointICA approach to estimate the weighting matrices for all three stimulus conditions simultaneously. In the discussion of our results, we emphasize the comparison between the two contour conditions (GO and LG), which is of most importance to this particular study.

Unimodal EEG and fMRI data analyses

In this section, we describe the results of a unimodal analysis of (simultaneously recorded) EEG or fMRI data, thereby ignoring the other modality. Fig. 2 graphically presents the condition-specific ERP and fMRI signals, averaged across subjects. The top panel of Fig. 2 shows the grand average ERPs on channel Oz for each stimulus condition. The shaded area represents the standard deviation across subjects. The scalp distributions of these grand average ERPs are displayed in the middle panel, at a latency of 90 ms (top) and 190 ms (bottom) after stimulus onset. The bottom panel shows fMRI results of a second-level SPM analysis on a lateral and medial view of an inflated template brain. The colored lines in these same figures represent the borders of the group ROIs V1, V2 and LOC. For this and all subsequent figures we only show the right hemisphere, because we could not reliably define the left hemisphere's ROIs in all participants. The T-scores, alongside with the MNI values of the strongest activated voxel in a particular area in the bottom panel of Fig. 2, are given in Table 1.

The grand mean ERPs in the top panel of Fig. 2 display a distinct pattern that is similar across conditions. The shape of these waveforms is typical for visual evoked potentials, with a first positive deflection at about 100 ms (P1), followed by a negativity between 150 and 200 ms (N1). The topography in the middle panel reveals that these deflections are mainly located over occipital electrode sites. These observations are in line with the results of a previous study where we measured the EEG response to similar Gabor displays outside the scanner (Machilsen et al., 2011). The fMRI maps in the bottom panel show activity in occipital and occipitotemporal regions. All three stimulus conditions activate areas V1 and V2, as well as the lateral occipital complex. Several fMRI studies have previously reported that both retinotopic and occipitotemporal areas are involved in contour integration (e.g., Altmann et al., 2003; Kourtzi et al., 2003). The results of our unimodal fMRI analysis are consistent with the univariate analyses reported by Schwarzkopf et al. (2009). Their contrast between collinear stimuli (comparable to our LG condition) and jittered stimuli (comparable to our NC condition) only revealed differences in higher visual areas (including object-sensitive regions), not in early visual areas.

By looking at the pair-wise contrasts shown in Fig. 3, we find that both LG and GO differ only in LOC compared to NC (Kourtzi et al., 2003). No clear difference in fMRI activity is observed between the LG and GO conditions. From this unimodal analysis we could conclude that both stimulus types are processed in a similar fashion. However, the LG and GO conditions do have a different ERP waveform, with the largest difference at about 200 ms. The difference in ERP suggests that

Table 1
The T-scores, alongside with the MNI coordinates of the strongest activated voxel for the 2nd level SPM analysis from the bottom panel of Fig. 2.

	Area	MNI	T-Scores
LG	EVA	11, −94, −3	14
	LOC	39, −87, −1	11.8
GO	EVA	9, −94, 5	13.2
	LOC	35, −85, 4	12
NC	EVA	12, −94, −3	8.4
	LOC	30, −92, 5	9.9

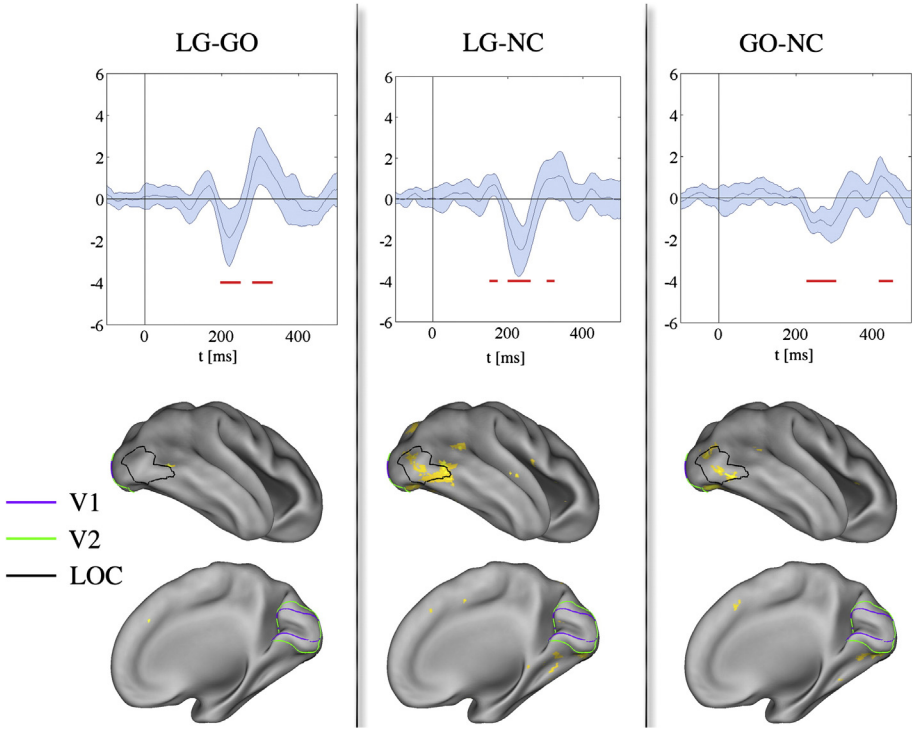


Fig. 3. Group-level differences between our three experimental conditions. From left to right: LG–GO, LG–NC, GO–NC. Top panel: ERP difference waves for electrode Oz. The shaded area represents 1.96 standard errors. Bottom panel: differences between fMRI PSC maps ($p = 0.01$, uncorrected) plotted on an inflated MNI template. The borders of our group ROIs V1, V2 and LOC are drawn as solid lines.

the processing of LG and GO stimuli is not identical, but that different processes (maybe even in different brain areas) are involved at different time points. The difference in fMRI suggests that the difference between LG and NC is larger than the difference between GO and NC, especially in the more anterior parts of LOC. The goal of the multimodal analysis is to unravel this spatiotemporal pattern further.

Multimodal analysis using JointICA

The JointICA results are shown in Figs. 4–6 for the conditions LG, GO and NC, respectively. As explained above, for each case, the stability index *Iq* from the ICASSO analysis was computed for the complete dataset as well as after leaving out one participant. In all cases, the

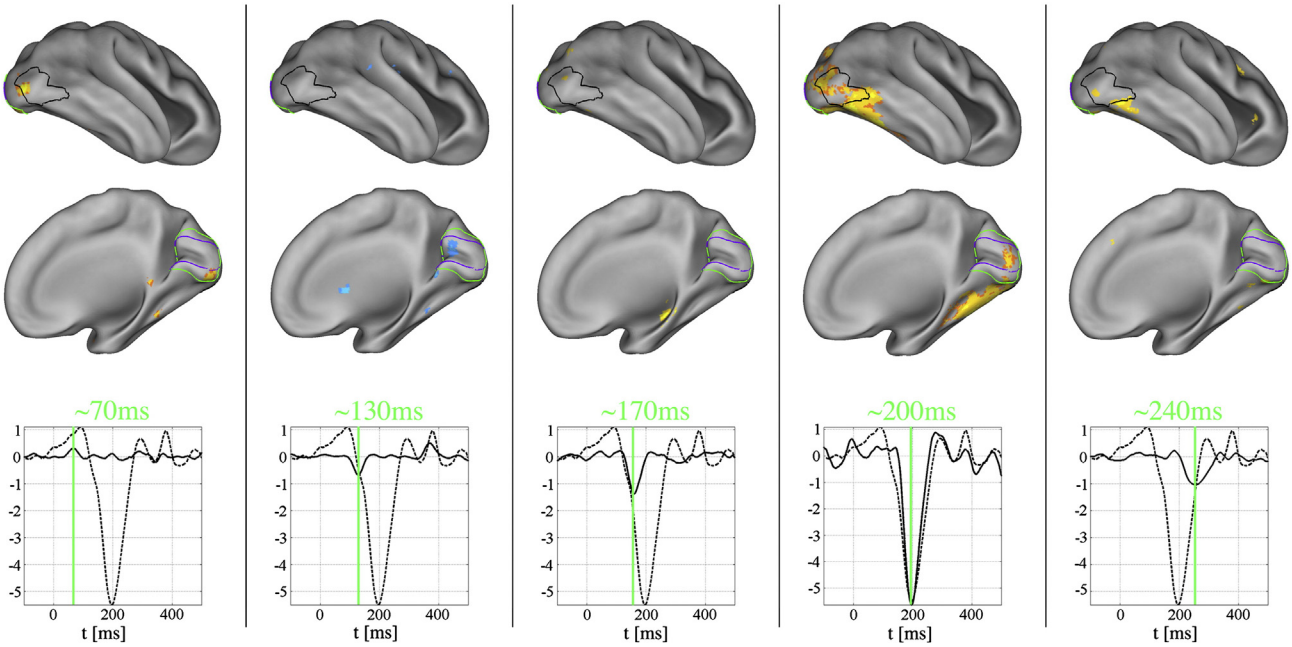


Fig. 4. Results of the JointICA analysis applied to the data in response to the LG stimulus. Five different components are shown, ordered according to their temporal contribution. For each component the upper panel of the figure shows the spatial (fMRI) part, whereas the bottom panel represents the temporal (ERP) part together with the average ERP waveform (solid versus dotted line, respectively). The fMRI figures show yellow-orange colors for positive activations and blue ones for deactivations and also include the contours of the ROIs of interest in the same colors as in Fig. 2. Only activations, of which the absolute value exceeds 3 times the standard deviation of the activation values in all voxels, are shown.

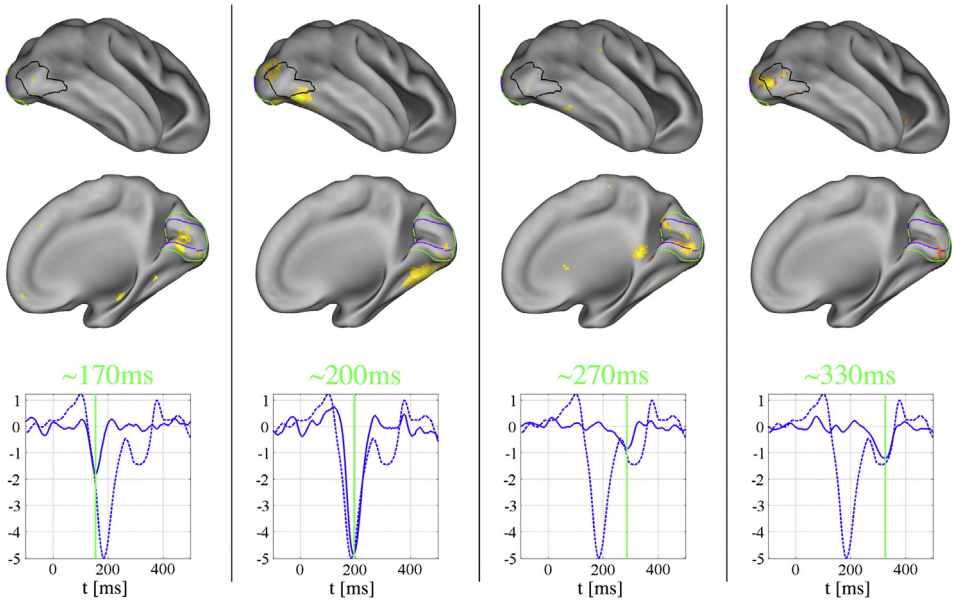


Fig. 5. Results of the JointICA analysis applied to the data in response to the GO stimulus. Four different components are shown, ordered according to their temporal contribution. For each component the upper panel of the figure shows the spatial (fMRI) part, whereas the bottom panel represents the temporal (ERP) part together with the average ERP waveform (solid versus dotted line, respectively). The fMRI figures show yellow-orange colors for positive activations and blue ones for deactivations and also include the contours of the ROIs of interest in the same colors as in Fig. 2. Only activations, of which the absolute value exceeds 3 times the standard deviation of the activation values in all voxels, are shown.

calculated values were higher than 0.9, implying a good reliability of the obtained results. The R-index of the ICASSO analysis estimated that we need to derive 15 components in order to have a stable decomposition, for all three conditions in this study. This does not imply, however, that all the 15 components were meaningful. The time-points shown in the figures and discussed below are solely determined by the JointICA method.

Fig. 4 shows both the temporal (ERP) and spatial (fMRI) part of five back-reconstructed independent components resulting from applying JointICA to the data from the LG condition. Together with the ERP part

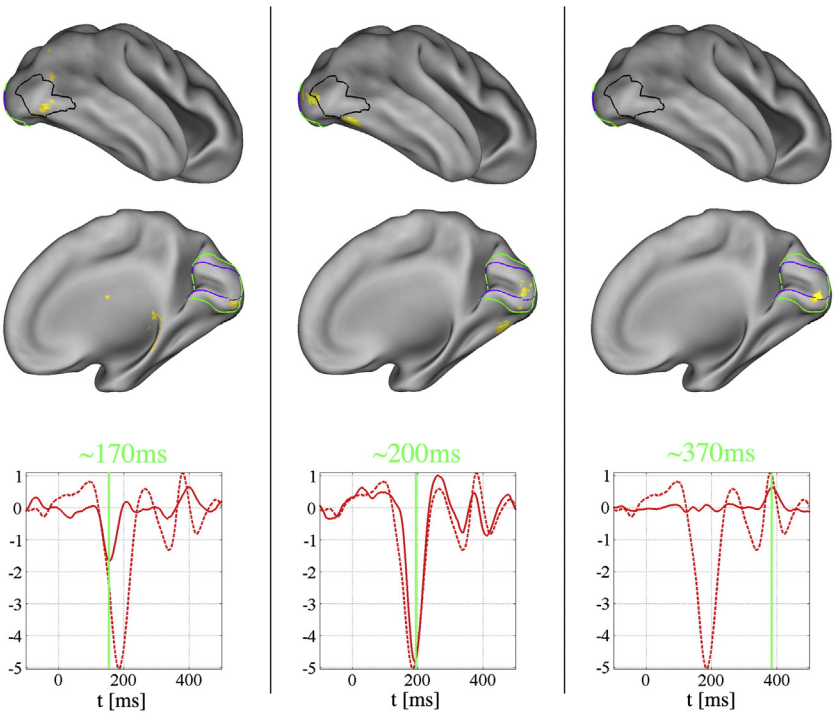


Fig. 6. Results of the JointICA analysis applied to the data in response to the NC stimulus. Three different components are shown, ordered according to their temporal contribution. For each component the upper panel of the figure shows the spatial (fMRI) part, whereas the bottom panel represents the temporal (ERP) part together with the average ERP waveform (solid versus dotted line, respectively). The fMRI figures show yellow-orange colors for positive activations and blue ones for deactivations and also include the contours of the ROIs of interest in the same colors as in Fig. 2. Only activations, of which the absolute value exceeds 3 times the standard deviation of the activation values in all voxels, are shown.

of the independent components, also the grand average ERP corresponding to this same condition is shown. The components are ordered according to their temporal behavior.

From this figure, it becomes clear that in the LG condition both V1 and V2 (together referred to as the early visual areas or EVA) are activated around 70 ms and 200 ms (panels 1 and 4, respectively). The LOC area is mainly activated around 200 ms (panel 4) but also around 70 ms and 170 ms (panels 1 and 3). In addition, negative visual activations are visible around 130 (panel 2). These negatively activated areas indicate that the ERP and fMRI components are "anti-correlated", meaning that larger ERP peaks correspond to smaller fMRI activations and vice-versa.

In a similar way as for the LG condition in Fig. 4, Fig. 5 shows the JointICA results from the data corresponding to the GO condition. For this condition, EVA activations are mainly found around 170 ms, 200 ms and 270 ms (panels 1, 2 and 3). Furthermore, the component found around 330 ms (panel 4) also shows additional EVA activation at this latency corresponding with a small peak at 70 ms. LOC activations are visible around 200 ms and 330 ms (panels 2 and 4). The activations around 200 ms are very similar to the activations shown earlier in Fig. 4, but there is a clear difference visible in the ERPs around 330 ms. More specifically, at this latency there is a clear negative peak for the GO condition, which cannot be seen in the LG results. For the GO condition, this peak corresponds to activations in LOC and EVA.

The JointICA results for the NC condition are summarized in Fig. 6. Also here, both the temporal and spatial parts of the independent components are shown, the former together with the grand average ERP waveform. Here, EVA activations are found around 170 ms, 200 ms and 370 ms (panels 1, 2 and 3) and LOC activations around 170 ms and 200 ms (panels 1 and 2). The late activation (around 370 ms) of the EVA ROI was also present for the LG condition (see Fig. 4, panel 2), but in the case of the LG condition, the relation between ERP and fMRI activations was negative, whereas for the current condition (NC) it is positive.

Multimodal analysis using modified JointICA

To surpass qualitative, visual comparison between the JointICA results for the three stimulus conditions, Fig. 7 illustrates the results of applying the modified JointICA approach to the data from all conditions simultaneously. The overview of the MNI coordinates of the peak activations for the corresponding maps is provided in Table 2. The number of independent sources to be derived was estimated to be 23. Six out of these 23 survived the energy-based selection criterion and are shown in Fig. 7. The upper part of the figure shows (from top to bottom) the condition-specific fMRI results for the LG, GO and NC condition, respectively. The condition-specific ERP results are shown below in the figure, together with their grand average ERP waveforms. Similar to Figs. 4–6, back-reconstructed components are shown. However, in this case, back-reconstruction is done with only the condition-specific part of the mixing matrix. This allows the independent components, although estimated together, to differ between conditions. For example, the first column in Fig. 7 shows the back-reconstruction of a source active around 70 ms. After condition-specific back-reconstruction, this source shows in both LG and GO conditions a similar positive deflection around 70 ms in the ERP, and significant activation in early visual areas in fMRI. However, we were unable to detect this component in NC condition. So at this point in time, similar sources are active in both contour conditions. The fifth column, describing the source active around 300 ms, shows clear differences after back-reconstruction. In the ERP, the back-reconstructed activity shows flat lines in LG and NC conditions, while a deflection is observed in the GO. This difference is due to the fact that the mixing vector for the LG and NC conditions contains very small values. The fMRI panels show active voxels for the GO condition, while no activations survived the threshold in the two other conditions. This implies that this source is unique to the GO condition. As explained before, a paired *t*-test is used to compare the condition-specific distributions across subjects for each component. The distributions, in this case, are the condition-specific columns of the mixing matrix, obtained by JointICA. In the figure, only *p*-values corresponding to significantly different distributions across subjects ($p < 0.05$) are included. Their subscripts specifically indicate the two conditions that were compared. In this way, we detect processes specific for only one or two conditions, as described in the Methods section.

The components in the first and third panel show the same distribution across subjects for the three conditions ($p > 0.05$). The component in the first panel shows activations in the early visual areas (EVA) around 70 ms after stimulus onset. This activation could not be separated in the original JointICA analysis for the NC and GO conditions (Figs. 5 and 6). The component in the third panel reveals activations in higher visual areas (LOC) around 200 ms. This same component was also found in the results obtained with the original JointICA analysis for all conditions (as shown in Figs. 4–6).

The component in the second panel shows activations in the LOC and EVA ROIs around 170 ms after stimulus onset. Similar to the component shown in panel 3, also this component was found in the individual JointICA analyses for all conditions (see Figs. 4–6). However, as opposed to this previously explained component, the distribution across subjects of the current one is significantly different for the LG and NC conditions, implying that the processes behind these activations are physiologically different. By closer look at the activated regions, it is obvious that, although the EVA and LOC ROIs are activated for all three conditions, the activation in the LOC is comparable for LG and GO, but different from NC. Also the activation of the EVA region is similar for LG and GO, but different for the NC condition. Although the difference between the ERP shapes is not apparent, their strengths are significantly different between these conditions.

The component presented in the fourth panel of Fig. 7, with the ERP part peaking around 240 ms after stimulus onset, shows significantly different distributions across subjects for all three conditions. The NC-specific ERP part of this IC is a flat line with zero amplitude, implying no activation for this condition around this latency. The difference between the GO- and LG-specific parts of this IC is in the amplitude of their ERP peaks at 240 ms. In addition, the GO condition shows activations in the EVA areas, whereas for the LG condition, also the LOC area is activated.

The fifth panel of Fig. 7 shows a component around 300 ms that is the only characteristic for the GO condition, with activations in the LOC and EVA ROIs. This component corresponds to a component retrieved with the individual JointICA analysis for this condition, as can be seen from panel 4 in Fig. 5. The advantage of the modified JointICA analysis, however, is that the flat lines available from the LG- and NC-specific parts of the ERP information confirm the exclusiveness of this component for the GO condition.

Finally, the rightmost panel of Fig. 7 shows an IC around 370 ms with not significantly different distributions across subjects for the three conditions. All three conditions reveal activations in the EVA areas. However, the EVA ROI activations for the NC and GO conditions are positive, whereas these same activations are negatively related to the ERP waveforms for the LG condition. This observation could not be made based on the results from the individual JointICA analyses and suggests the presence of very late activations of the early visual areas specifically for GO and NC.

Discussion

In the present study we investigated the temporal interactions between brain regions involved in contour integration and shape detection. Because a unimodal analysis of EEG and fMRI data is not able to unravel the full dynamics of the processes involved, we present an integrated analysis of EEG and fMRI data that can reveal the spatiotemporal differences between different perceptual processes induced by different

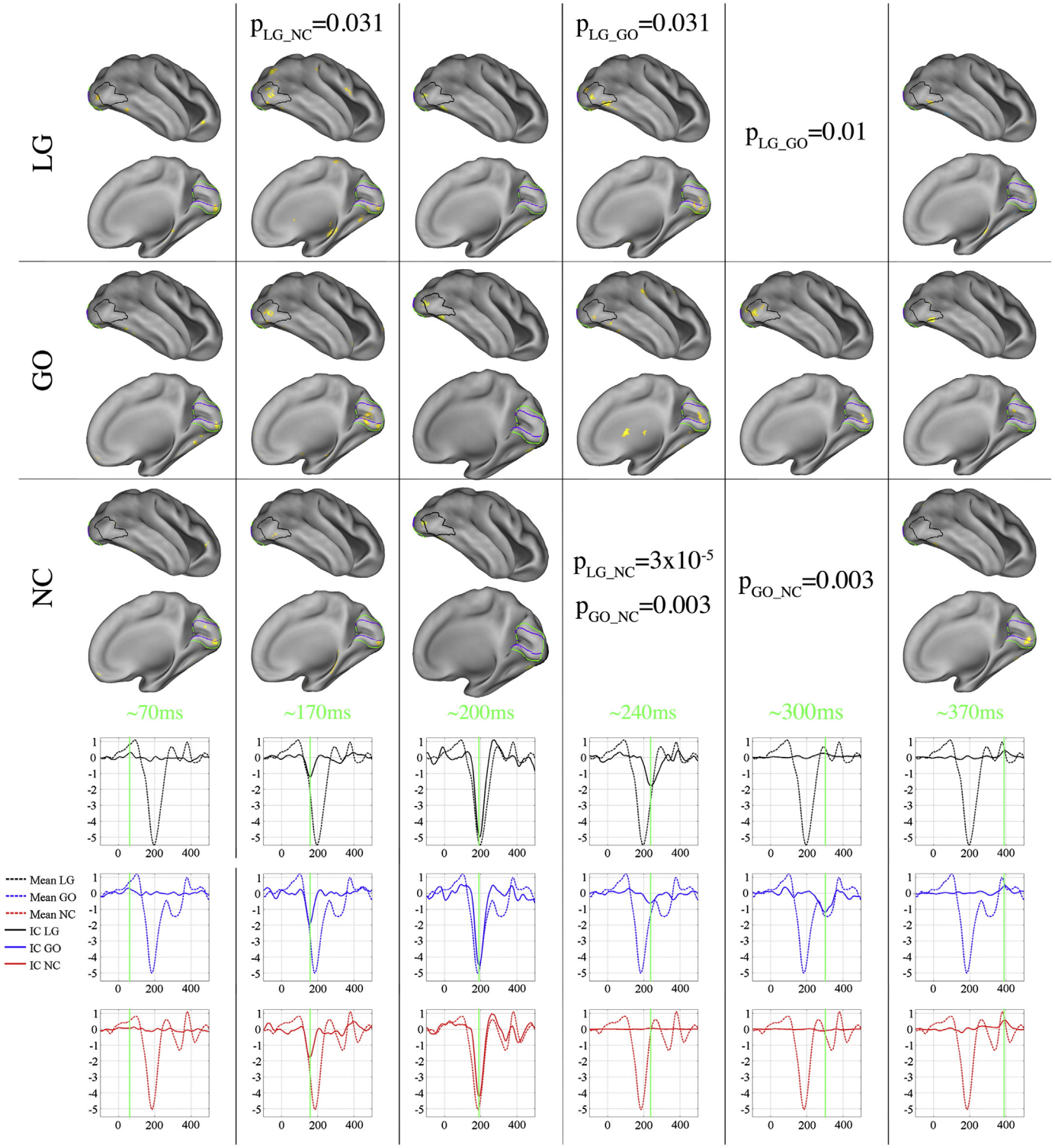


Fig. 7. Results of the modified JointICA analysis, performed jointly on the data from all three conditions (LG = local and global, GO = global only and NC = no contour). The upper panels show the spatial (fMRI) results from the condition-specific independent components, for (from top to bottom) the LG, GO and NC conditions. For each case, the results are only depicted from those angles that show the major part of the activation (as before, only those parts of the activation are shown that exceed 3 times the standard deviation of all activation values). *p*-Values are only mentioned if they are below 0.05. The bottom panel presents the temporal (ERP) parts of the independent components, with different colors distinguishing between the different conditions. These colors correspond to those used in Figs. 4–6. Together with the independent components (solid line), also the grand average ERPs for all conditions are plotted (dashed line). Like in Figs. 4–6, also here the components are ordered according to their temporal peak behavior. The empty fMRI sections in panels 4 and 5 correspond to components for which the ERP part is a flat line.

stimulus conditions. Integration of EEG and fMRI data can be achieved in several ways. We opted to apply JointICA as it provides an elegant way to extract sources that link peaks separated in the EEG to regions in the fMRI based on across-subject variability. As the original method would decompose an EEG–fMRI dataset for each condition separately, we also modified the JointICA approach to estimate weighting matrices simultaneously for all stimulus conditions. With this modification, the method is able to pinpoint where and when different stimulus types

Table 2
The overview of the signal strength expressed in the multiples of standard deviation of the signal, alongside with the MNI coordinates of the peak activation corresponding to the maps shown in Fig. 7. The MNI coordinates are provided for each ROI per component per condition.

Component	Condition	Strength	MNI Coordinates	ROI
70 ms	LG	4.4	15, −93, 12	EVA
		3.35	36, −90, −7	LOC
	GO	4.39	13, −96, −2	EVA
			–	LOC
	NC	4.16	12, −91, −10	EVA
			–	LOC
170 ms	LG	4.67	14, −91, −11	EVA
		3.9	44, −83, −7	LOC
	GO	4.87	14, −91, −11	EVA
		4.73	41, 85, −6	LOC
	NC	5.74	14, −92, −11	EVA
		3.8	41, −75, −13	LOC
200 ms	LG		–	EVA
		5.74	34, −90, −3	LOC
	GO		–	EVA
		5.56	35, −90, −6	LOC
	NC		–	EVA
		5.84	34, −90, −6	LOC
240 ms	LG	3.7	11, −90, −11	EVA
		3.91	39, −85, −10	LOC
	GO	3.23	11, −94, −5	EVA
		3.17	37, −82, −14	LOC
	NC		–	EVA
			–	LOC
330 ms	LG		–	EVA
			–	LOC
	GO	4,61	11, −92, 15	EVA
		5.43	40, −86, −6	LOC
	NC		–	EVA
			–	LOC
370 ms	LG	3.71	12, 95, −2	EVA
		3.71	39, −71, −14	LOC
	GO	5.21	7, −76, 12	EVA
		4.82	39, −71, −14	LOC
	NC	5.89	10, −91, −6	EVA
			–	LOC

elicited similar or distinct patterns of activity. In addition, the modified JointICA method allows for a quantitative comparison of individual components in a principled and unbiased way. Results from the modified JointICA confirm earlier findings but also provide novel insights in how perceptual grouping happens in the visual system, especially in combination with shape perception.

Let us start with a summary of the findings from the original JointICA (Figs. 4–6). In the LG condition, the strong N1 from the ERP waveform is captured quite well with an IC reflecting widespread activation in the LOC around 200 ms after stimulus onset. This peak is seen to build up from 70 ms onwards with activity shifting forwards along the ventral stream. In the GO condition, where the global shape is more difficult to see because it is not supported by simple pairwise contour linking between neighboring Gabor elements, ventral stream activity emerges later in time, with much weaker LOC activation throughout. Moreover, this condition induces a much later negative peak around 330 ms, involving a loop between LOC and EVA, which was completely absent in the LG condition. At this stage, an information exchange between EVA and LOC is probably taking place to establish a shape percept at a higher level (LOC), while trying to use as many of the oriented elements (signaled in EVA) as possible, which are compatible with a globally closed contour. In the NC condition, where no contour, neither locally nor globally defined, is present whatsoever, activations are still weaker and a small positive peak arises quite late after stimulus onset (around 370 ms), which appears to be accompanied by EVA activity again.

The results clearly show that the visual processing of a contour-defined shape is not merely a spatiotemporal shift of activity from early retinotopic to later occipitotemporal areas. Rather, it involves a dynamic interplay between these areas, in which the exact areas involved and the dynamics of their interplay depend on the specific stimulus condition. The modified JointICA allows to visualize this interplay in a more refined way. Focusing on the results shown in Fig. 7, visual processing starts in V1–V2 around 70 ms, shifting forward to higher visual areas in the ventral stream around 170 ms. Around 240 ms, clear differences between the stimuli with structure (LG and GO) and the stimuli without structure (NC) appear. These results are consistent with earlier EEG studies (e.g., Machilsen et al., 2011; Mathes et al., 2006) and MEG studies (e.g., Tanskanen et al., 2008). This indicates that the first percept of some kind of structure that stands out from the background is accomplished around that time. However, that does not mean that processing stops at that point. At least in the condition where the shape is less well defined (the GO condition) because local edge linking is insufficient, an additional feedback loop occurs around 300 ms, which entails a reactivation of EVA. This could be interpreted as re-entrant processing where the visual system checks whether the local Gabor elements that form part of the groups established further in the cortical hierarchy are really belonging to the same global shape represented in the LOC. The activations in V1 and V2 at such a later stage could indicate that (at least half of) the elements are not really locally "fitting" with the predictions generated at higher levels in the cortical hierarchy but only as a subset that fits a larger group in a hierarchical fashion, much as small Ls forming larger Hs in the Navon type of hierarchical stimuli (for reviews, see Kimchi, 1992; Navon, 2003). In the condition without a contour (NC) yet a later peak emerges, which also reflects EVA activity. This could reflect attentional enhancement as part of an attempt to verify whether there is really no structure there.

Consistent with previous findings in neurophysiology (Angelucci et al., 2002; McManus et al., 2011; Zhang and von der Heydt, 2010) and in human fMRI studies (Altmann et al., 2003; Kourtzi et al., 2003; Schwarzkopf et al., 2009), our results confirm the role of recurrent processing between high-level shape and object areas such as LOC and low-level retinotopic areas such as V1 and V2 in the integration of local elements into a global shape with a closed contour. A number of recent studies using fMRI have attempted to reveal how global shapes emerge from local elements along the cortical hierarchy, using fMRI adaptation (e.g., Kourtzi and Huberle, 2005) and fMRI multi-voxel pattern analysis or MVPA (e.g., Kubilius et al., 2011; Ostwald et al., 2008; Schwarzkopf et al., 2009). Although these studies differed widely with respect to the stimuli and tasks they employed, the overall conclusions were uniformly pointing towards sensitivity for local element attributes in the early visual areas and for global structure and shape properties in the higher occipitotemporal areas. However, the sluggish temporal resolution of fMRI did not allow to draw conclusions about the temporal dynamics of the information flow between these more locally interested areas and these more globally interested areas.

Mayhew et al. (2012) have recently used simultaneous EEG–fMRI measurements to unravel the spatiotemporal dynamics within the extended network involved in learning to discriminate different types of global structures in dot patterns with variable noise levels. Using MVPA on the activations in the regions identified by EEG-informed fMRI mapping, these authors were able to distinguish learning in early processes involved in integration of local signals into more global forms in occipitotemporal and parietal areas from learning in later processes related to categorical decision making in frontal circuits. We used a different form of integrated fMRI-EEG data analysis, JointICA, for a different purpose. We wanted to understand the interplay between more local image analysis in the retinotopic visual areas and more global shape analysis in higher areas, and how this changes over time depending on the nature of the stimulus. We found that a more difficult type of structure emerges later in time and requires a more elaborate information exchange between lower and higher areas. We believe that such an iterative process plays a key role in extracting structure and constructing shape representations from natural images too, where

clutter, noise, and occlusion all add to the complexity of contour integration.

In general, our findings fit quite well with more recent alternative views on the nature of the cortical hierarchy. Rather than assuming that there is always a fixed feedforward flow, which goes sequentially through all the stages along the ventral stream, low- and high-level areas do not necessarily engage exclusively in early and late aspects of processing, respectively. This view was made quite explicit in Hochstein and Ahissar's (2002) Reverse Hierarchy Theory, which involves a fast feedforward sweep, generating global percepts and high-level interpretation of the gist of the scene, followed by slower recurrent processing, integrating the local details within these top-down generated percepts when the task requires the fine resolution available at lower areas. Hence, early processing can occur at high levels in the visual system and low-level areas can be active during late processing (see also Lee et al., 1998; Roelfsema, 2006). A second larger theoretical framework that is consistent with our results is predictive coding (e.g., Friston, 2010; Rao and Ballard, 1999), which has already inspired a lot of interesting empirical work, both with fMRI (e.g., Alink et al., 2010; Fang et al., 2008; but see de-Wit et al., 2010, 2012 for discussion) and with neurophysiologically detailed models (Spratling, 2010). In short, the idea is that visual cortex is continuously updating its predictions about the world, which are generated at higher levels, with only the mismatches or prediction errors being transmitted from low- to high-level areas. In terms of our study, this view would imply more activity in low-level areas in the more difficult condition with shapes defined only globally, with locally neighboring elements not being aligned and not fitting the global shape at the lower level in the hierarchy, which is exactly what we found. However, because this interpretation is largely speculative at this point, it awaits further confirmation from additional experiments specifically designed to test it.

Acknowledgments

We thank Jessica Bulthé and Christophe Bossens for assisting in the data collection, Ron Peeters for the technical support during scanning, and Annelies Baeck, Vanja Van Aarsen and Peter Stiers for their help in the ROI definitions. We also thank the editor and the reviewers for comments that helped to improve the paper. This research is supported by the Research Council KUL: IDO/05/010 (EEG–fMRI integration), GOA MaNet and PFV/10/002 (OPTEC); IUAP P719 (DYSCO, 2012–2017); the Flemish Government: FWO project G.0427.10N Integrated EEG–fMRI, IWT-TBM080658-MRI (EEG–fMRI) and iMinds. B. Mijović is supported by a PDM postdoctoral fellow of KU Leuven, Belgium. B. Machilsen is a postdoctoral fellow of the Research Foundation-Flanders. M. De Vos is supported by an Alexander von Humboldt grant and J. Wagemans by long-term structural funding from the Flemish Government (METH/08/02).

References

Alink, A., Schwiedrzik, C.M., Kohler, A., Singer, W., Muckli, L., 2010. Stimulus predictability reduces responses in primary visual cortex. J. Neurosci. 30, 2960–2966.
Allen, P., Josephs, O., Turner, R., 2000. A method for removing imaging artifact from continuous EEG recorded during functional MRI. NeuroImage 12, 230–239.
Altmann, C.F., Bülthoff, H.H., Kourtzi, Z., 2003. Perceptual organization of local elements into global shapes in the human visual cortex. Curr. Biol. 13 (4), 342–349.
Angelucci, A., Bressloff, P.C., 2006. Contribution of feedforward, lateral and feedback connections to the classical receptive field center and extra-classical receptive field surround of primate V1 neurons. Prog. Brain Res. 154, 93–120.
Angelucci, A., Levitt, J.B., Walton, E.J., Hupé, J.M., Bullier, J., Lund, J.S., 2002. Circuits for local and global signal integration in primary visual cortex. J. Neurosci. 22, 8633–8646.
Calhoun, V.D., Adali, T., Pearlson, G.D., Kiehl, K.A., 2006. Neuronal chronometry of target detection: fusion of hemodynamic and event-related potential data. NeuroImage 30, 544–553.
De Vos, M., De Lathauwer, L., Van Huffel, S., 2011. Spatially constrained ICA algorithms with applications in EEG processing. Signal Process. 91 (8), 1963–1972.
Delorme, A., Makeig, S., 2004. EEGLAB: an open source toolbox for analysis of single-trial EEG dynamics including independent component analysis. J. Neurosci. Methods 134, 9–21.
Demeyer, M., Machilsen, B., 2012. The construction of perceptual grouping displays using GERT. Behav. Res. Methods 44 (2), 439–446.
de-Wit, L.H., Machilsen, B., Putzeys, T., 2010. Predictive coding and the neural response to predictable stimuli. J. Neurosci. 30, 8702–8703.
de-Wit, L.H., Kubilius, J., Wagemans, J., Opde Beeck, H.P., 2012. Bi-stable Gestalts reduce activity in the whole of V1 not just the retinotopically predicted parts. J. Vis. 12 (11), 1–14. http://dx.doi.org/10.1167/12.11.12 (12).
Elder, J.H., Goldberg, R.M., 2002. Ecological statistics of Gestalt laws for the perceptual organization of contours. J. Vis. 2 (4), 324–353 (5).
Fang, F., Kersten, D., Murray, S.O., 2008. Perceptual grouping and inverse fMRI activity patterns in human visual cortex. J. Vis. 8 (7), 1–9. http://dx.doi.org/10.1167/8.7.2 (2).
Field, D.J., Hayes, A., Hess, R.F., 1993. Contour integration by the human visual system: evidence for a local "association field". Vis. Res. 33, 173–193.
Friston, K., 2010. The free-energy principle: a unified brain theory? Nat. Rev. Neurosci. 11 (2), 127–138.
Geisler, W.S., 2008. Visual perception and the statistical properties of natural scenes. Annu. Rev. Psychol. 59, 167–192.
Gläscher, J., 2009. Visualization of group inference data in functional neuroimaging. Neuroinformatics 7, 73–82.
Grill-Spector, K., Kushnir, T., Hendler, T., Edelman, S., Itzchak, Y., Malach, R., 1998. A sequence of object-processing stages revealed by fMRI in the human occipital lobe. Hum. Brain Mapp. 6, 316–328.
Hess, R.F., Field, D.J., 1999. Integration of contours: new insights. Trends Cogn. Sci. 3, 480–486.
Himberg, J., Hyvärinen, A., Esposito, F., 2004. Validating the independent components of neuroimaging time-series via clustering and visualization. NeuroImage 22, 1214–1222.
Hochstein, S., Ahissar, M., 2002. View from the top: hierarchies and reverse hierarchies in the visual system. Neuron 36, 791–804. http://dx.doi.org/10.1016/S0896-6273(02)01091-7.
Huster, R.J., Debener, S., Eichele, T., Herrmann, C.S., 2012. Methods for simultaneous EEG–fMRI: an introductory review. J. Neurosci. 32 (18), 6053–6060.
Joyce, C., Gorodnitsky, I., Kutas, M., 2004. Automatic removal of eye movement and blink artifacts from EEG data using blind component separation. Psychophysiology 41 (2), 313–325.
Kao, M., Mandal, A., Lazar, N., Stufken, J., 2009. Multi-objective optimal experimental designs for event-related fMRI studies. NeuroImage 44, 849–856.
Kimchi, R., 1992. Primacy of wholistic processing and global/local paradigm: a critical review. Psychol. Bull. 112, 24–38.
Kourtzi, Z., Huberle, E., 2005. Spatiotemporal characteristics of form analysis in the human visual cortex revealed by rapid event-related fMRI adaptation. NeuroImage 28, 440–452.
Kourtzi, Z., Tolias, A.S., Altmann, C.F., Augath, M., Logothetis, N.K., 2003. Integration of local features into global shapes: monkey and human fMRI studies. Neuron 37 (2), 333–346.
Kubilius, J., Wagemans, J., Opde Beeck, H.P., 2011. Emergence of perceptual Gestalts in the human visual cortex: the case of the configural superiority effect. Psychol. Sci. 22, 1296–1303. http://dx.doi.org/10.1177/0956797611417000.
Lee, T.S., Mumford, D., Romero, R., Lamme, V.A.F., 1998. The role of the primary visual cortex in higher level vision. Vis. Res. 38, 2429–2454. http://dx.doi.org/10.1016/S0042-6989(97)00464-1.
Li, W., Gilbert, C.D., 2002. Global contour saliency and local colinear interactions. J. Neurophysiol. 88, 2846–2856.
Machilsen, B., Noviskiy, N., Vancleef, K., Wagemans, J., 2011. Context modulates the ERP signature of contour integration. PLoS ONE 6 (9), e25151.
Mathes, B., Trenner, D., Fahle, M., 2006. The electrophysiological correlate of contour integration is modulated by task demands. Brain Res. 1114 (1), 98–112.
Mayhew, S.D., Li, S., Kourtzi, Z., 2012. Learning acts on distinct processes for visual form perception in the human brain. J. Neurosci. 32 (3), 775–786.
McManus, J.N.J., Li, W., Gilbert, C.D., 2011. Adaptive shape processing in primary visual cortex. Proc. Natl. Acad. Sci. U. S. A. 108, 9739–9746.
Mijović, B., Vanderperren, K., Novitskiy, N., Vanrumste, B., Stiers, P., Van den Bergh, B., Wagemans, J., Lagae, L., Sunaert, S., Van Huffel, S., De Vos, M., 2012. The "why" and "how" of JointICA: results from a visual detection task. NeuroImage 60, 1171–1185.
Moosmann, M., Schonfelder, V., Specht, K., Scheeringa, R., Nordby, H., Hugdahl, K., 2009. Realignment parameter-informed artefact correction for simultaneous EEG–fMRI recordings. NeuroImage 45, 1144–1150.
Navon, D., 2003. What does a compound letter tell the psychologist's mind? Acta Psychol. 114, 273–309.
Niazy, R., Beckmann, C., Iannetti, G., Brady, J., Smith, S., 2005. Removal of fMRI environment artifacts from EEG data using optimal basis sets. NeuroImage 28, 720–737.
Ostwald, D., Lam, J.M., Li, S., Kourtzi, Z., 2008. Neural coding of global form in the human visual cortex. J. Neurophysiol. 99, 2456–2469.
Rao, R.P.N., Ballard, D.H., 1999. Predictive coding in the visual cortex: a functional interpretation of some extra-classical receptive-field effects. Nat. Neurosci. 2 (1), 79–87. http://dx.doi.org/10.1038/4580.
Roelfsema, P.R., 2006. Cortical algorithms for perceptual grouping. Annu. Rev. Neurosci. 29, 203–277. http://dx.doi.org/10.1146/annurev.neuro.29.051605.112939.
Schwarzkopf, D.S., Zhang, J., Kourtzi, Z., 2009. Flexible learning of natural statistics in the human brain. J. Neurophys. 102, 1854–1867.
Spratling, M.W., 2010. Predictive coding as a model of response properties in cortical area V1. J. Neurosci. 30, 3531–3543.
Tanskanen, T., Saarinen, J., Parkkonen, L., Hari, R., 2008. From local to global: cortical dynamics of contour integration. J. Vis. 8 (7:15), 1–12.
Vanderperren, K., De Vos, M., Ramautar, J.R., Novitskiy, N., Mennes, M., Assecondi, S., Vanrumste, B., Van den Bergh, B.R., Wagemans, J., Lagae, L., Sunaert, S., Van Huffel, S., 2010. Removal of BCG artifacts from EEG recordings inside the MR scanner: a

comparison of methodological and validation-related aspects. NeuroImage 50, 920–934.
Wagemans, J., Elder, J.H., Kubovy, M., Palmer, S.E., Peterson, M.A., Singh, M., von der Heydt, R., 2012. A century of Gestalt psychology in visual perception: I. Perceptual grouping and figure-ground organization. Psychol. Bull. 138, 1172–1217.
Wertheimer, M., 1923. Untersuchungen zur Lehre von der Gestalt. Psychol. Forsch. 4, 301–350.
Zhang, N.R., von der Heydt, R., 2010. Analysis of the context integration mechanisms underlying figure-ground organization in the visual cortex. J. Neurosci. 30, 6482–6496. http://dx.doi.org/10.1523/JNEUROSCI.5168-09.2010.